Development and Optimization of Regularized Tomographic Reconstruction Algorithms Utilizing Equally-Sloped Tomography

Yu Mao, Benjamin P. Fahimian, Stanley J. Osher, and Jianwei Miao

***Abstract*—We develop two new algorithms for tomographic reconstruction which incorporate the technique of equally-sloped tomography (EST) and allow for the optimized and flexible implementation of regularization schemes, such as total variation constraints, and the incorporation of arbitrary physical constraints. The founding structure of the developed algorithms is EST, a technique of tomographic acquisition and reconstruction first proposed by Miao *et al.* in 2005 for performing tomographic image reconstructions from a limited number of noisy projections in an accurate manner by avoiding direct interpolations. EST has recently been successfully applied to coherent diffraction microscopy, electron microscopy, and computed tomography for image enhancement and radiation dose reduction. However, the bottleneck of EST lies in its slow speed due to its higher computation requirements. In this paper, we formulate the EST approach as a constrained problem and subsequently transform it into a series of linear problems, which can be accurately solved by the operator splitting method. Based on these mathematical formulations, we develop two iterative algorithms for tomographic image reconstructions through EST, which incorporate Bregman and continuative regularization. Our numerical experiment results indicate that the new tomographic image reconstruction algorithms not only significantly reduce the computational time, but also improve the image quality. We anticipate that EST coupled with the novel iterative algorithms will find broad applications in X-ray tomography, electron microscopy, coherent diffraction microscopy, and other tomography fields.**

***Index Terms*—Bregman regularization, continuative regularization, equally-sloped tomography, operator splitting method, pseudo-polar Fourier transform.**

Manuscript received December 10, 2009; revised March 16, 2009. First published December 31, 2009; current version published April 16, 2010. This work was supported by the UC Discovery Grant IT107-10166, in conjunction with TomoSoft Technologies. The associate editor coordinating the review of this manuscript and approving it for publication was Prof. Ljubisa Stankovic.

Y. Mao is with the Department of Mathematics and Department of Physics and Astronomy, University of California, Los Angeles, CA 90095 USA (e-mail: ymao29@math.ucla.edu).

B. P. Fahimian is with the Department of Physics and Astronomy and Department of Radiation Oncology, University of California, Los Angeles, CA 90095 USA (e-mail: bfahimian@mednet.ucla.edu).

S. J. Osher is with the Department of Mathematics, University of California, Los Angeles, CA 90095 USA (e-mail: sjo@math.ucla.edu).

J. Miao is with the Department of Physics and Astronomy and the California Nano Systems Institute, University of California, Los Angeles, CA 90095 USA (e-mail: miao@physics.ucla.edu).

Color versions of one or more of the figures in this paper are available online at http://ieeexplore.ieee.org.

Digital Object Identifier 10.1109/TIP.2009.2039660

I. Introduction

TOMOGRAPHY has made revolutionary impacts in a number of fields ranging from biology to medicine [4]–[6]. While the applications of tomography are wide and diverse, the problems associated with its mathematical and experimental implementation are similar. On the one hand, an accurate image reconstruction is desired. On the other hand, the radiation dose imparted to biological specimens and the patient in computed tomography (CT) is a major concern [7]–[9]. It is, hence, a central problem to reconstruct a clean and faithful image from a limited number of noisy projection measurements. Such a reconstruction procedure can be treated as an ill-posed mathematical problem, and in general doesn't have a unique solution due to the lack of enough measurements and the presence of noise in the data. Conventional tomographic reconstruction methods [4], such as the well-known filtered back projection (FBP), the algebraic reconstruction technique (ART), and the simultaneous algebraic reconstruction technique (SART), uses interpolations either in object or Fourier domain, which unavoidably introduces noise in the reconstructed images [4], [6]. A postdenoising procedure may be applied to removing the noise in the reconstructed image, but also erases the fine features in the image and, hence, reduces the spatial resolution. In this paper, we develop novel algorithms to find the "best" possible solution to match the experimental measurements an physical constraints. Due to the incompleteness of experiential data and the presence of noise in the expediential measurement, there exists no perfect tomographic reconstruction. However, we utilize regularization functionals to quantify the quality of the reconstruction, and search for the most regularized image that is concurrently and strictly consistent with the experimental data and the physical constraints.

The method presented here is built upon a novel data acquisition procedure and a direct Fourier-based iterative reconstruction scheme, referred to as Equally-Sloped Tomography (EST) [1]. The EST method iterates back and forth between object and the Fourier domains where constraints are enforced in both domains. The EST iterative algorithm is based on a new form of the fast Fourier transform (FFT) called the pseudo-polar Fourier transform (PPFT) [10], [11], in which the grid points in the Fourier domain are lying on the equally-sloped lines instead of equally-angled lines. It has been mathematically shown that PPFFT is algebraically exact, geometrically faithful and invertible [10].

The EST method also uses another important scheme, called "oversampling", which was initially developed to solve the phase problem for noncrystallographic specimens [12]–[14].

When a Fourier slice is sampled at a frequency finer than the Nyquist interval, the corresponding projection in object domain is surrounded by mathematical zeros. If the Fourier slice calculated from the measured projections are oversampled, the 3-D object to be reconstructed should be surrounded with zeros. These mathematical zeros do not provide extra information about the 3-D object, but help to extract the correlated information among the Fourier slices. By using PPFFT and its inversion, an algorithm is developed to iterate back and forth between Fourier and object domains. In Fourier domain, the measured Fourier slices are updated in each iteration. In object domain, a support is defined to separate the object from its surrounding zeros, and the voxels outside the support and the negative voxels inside the support are set to zeros. The algorithm converges to a solution which satisfies the experiential measurements and the physical constraints the most. While the EST iterative algorithm makes superior image reconstructions, the bottleneck of the algorithm is the speed of the inverse PPFFT which is more than one order slower than the forward PPFFT and, hence, hinders its broad applications.

In this paper, we present mathematical formulation for the image reconstruction problem related to EST, and develop two iterative algorithms without use of the inverse PPFFT. By numerical experiments, we show that the new algorithms not only significantly reduce the computational time, but also improve the quality of the reconstructed images. The organization of the paper is as follows. In Section II, we give a theoretic account of the method and the iterative algorithms. In Section III, we provide the implementation of the algorithms. Numerical results are present in Section IV and the conclusion in Section V.

II. Theory

A. Mathematical Formulation

The EST projection data are ideally acquired at angles corresponding to the lines of the pseudo-polar grid, which consists of concentric squares with a horizontal and a vertical groups of lines, shown in Fig. 1. The purpose of such an acquisition, in conjunction with the proposed algorithms, is to provide a methodology to completely eliminate deleterious interpolations that that riddle conventional tomographic reconstruction algorithms. In both groups of lines on the pseudo-polar grid, the lines are aligned in a manner that the slopes of the lines form an arithmetic sequence, i.e., the difference of the slope between two consecutive lines is a constant (i.e., the lines are equally-sloped), whereas in the standard polar grid, the angle between two consecutive lines is a constant (i.e., the lines are equally-angled). The pseudo-polar grid was initially introduced by Mersereau *et al.* [15] for the purpose of image reconstruction. It was not until recently that a direct Fourier transform (i.e., PPFFT) was developed to relate the pseudo-polar and the Cartesian grids [10], [16].

The 2-D pseudo-polar Fourier transform, denoted by $\mathcal{F}$ throughout this paper, is defined between an $N \times N$ array in Cartesian grid and a pseudo-polar grid with $2N$ solid lines with each having $2N$ grid points, whereas each line represents a Fourier slice. A fast algorithm of such a transform has already been developed and can be implemented with the same complexity order as the standard FFT [10]. The adjoint pseudo-polar Fourier transform, denoted by $\mathcal{F}^\top$ throughout this paper, can be implemented with the same efficiency.

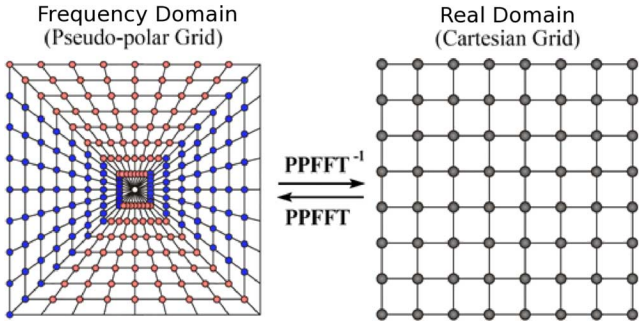

Fig. 1. Graphical relationship between the oversampled pseudopolar grid and the corresponding Cartesian grid, where $\mathrm{N} = 8$. Not all data at the pseudo-polar grid point are approachable, as we explained above.

However, there are several substantial differences between the PPFFT and the standard FFT. First of all, $\mathcal{F}$ itself is not orthogonal, i.e., $\mathcal{F}\mathcal{F}^\top \neq \mathcal{F}^\top\mathcal{F} \neq Id$. That is to say the adjoint transform is not equivalent with the inverse transform of $\mathcal{F}$. Second, the total number of the grid points in the frequency domain is four times more than the number of the corresponding grid points in the real domain, which means that the transform itself is "redundant". Therefore, an inverse transform is actually defined and implemented by solving the corresponding least square problem

$$\mathcal{F}^{-1}(v) := \arg\min_u \|\mathcal{F}u - v\|_2. \tag{1}$$

In [10], two numerical algorithms for the inversion of $\mathcal{F}$ are developed. Both of them have a much higher complexity than the forward transform itself. As a result, an efficient reconstruction scheme should avoid using the inverse pseudo-polar Fourier transform as much as possible.

Here, we mathematically formulate the problem discussed above. Let u be the 2-D image to be reconstructed in object domain. $\mathcal{F}u$ denotes the pseudo-polar Fourier transform of u.

The information we attained from the tomography data can be expressed as

$$S\mathcal{F}u = b_1 \tag{2}$$

where S is a linear operator selecting the entry of approachable frequency values and b_1 is an array in frequency domain that contains the known frequency values. This is the "frequency constraint". On the other hand, since we impose the oversampling method, the surrounding region of the image is known to be zero. Moreover, we might know some pixels in the object region with certain intensity values in practice. we can define the corresponding projection operator as S_0 and have the following "physical constraint"

$$S_0 u = b_0 \tag{3}$$

where b_0 contains the padded zero surrounding the image and other known object values. Comparing with condition (2), this constraint is more mathematically rigorous, and the unknowns in u are indeed directly eliminated here, so we can use this condition to simplify the matrix involved in the system (2). Notice

that (3) is equivalent with $u = (I - S_0)u + b_0$, where I is the identity matrix. Plug it into (2), then we have

$$S\mathcal{F}(I - S_0)u = b_1 + S\mathcal{F}b_0. \tag{4}$$

This system has a largely reduced rank comparing with (2). For simplicity, we denote the equation $S\mathcal{F}(I - S_0)u = b_1 + S\mathcal{F}b_0$ as $Au = b$ throughout this paper.

Since both (3) and (4) are linear equations, a direct least square solution can in principle be obtained, but such a solution is not necessarily an optimal one due to the presence of noise. In order to obtain a best possible solution, a regularization functional is needed to quantify the quality of the reconstructed image. In another word, we want to find a solution that optimizes the regularization functional and also satisfies equation (3) and (4). In this paper, we use the total variation norm to regularize the image, which is utilized in the ROF model, one of the most successful denoising models developed by Rudin *et al.* [17]. This model is widely recognized to be able to remove the noise and other unwanted fine scale artifacts while preserve sharp edges in an image by minimizing the total variation norm, which is defined as

$$\|u\|_{TV} := \int_{\Omega} |\nabla u(x)|\, dx. \tag{5}$$

We want to point out that other regularization functionals may also be utilized here and can perform well under certain conditions. For example, the nonlocal means regularization functional, developed by Buades *et al.* in [18], is proved to give good performance when the image contains periodic or repeating patterns. When replacing the regularization term, the whole structure of the analysis demonstrated in this paper remains the same and the direct extension of the algorithm is straight forward.

In the following sections, we focus on the constrained optimization problem

$$\min \|u\|_{TV} \quad \text{s.t.} \quad Au = b \tag{6}$$

where u is restricted in the subspace $\{u : S_0 u = b_0\}$, and only the unknown elements of u are free to change.

B. Algorithm Structure and Related Works

The constrained problem (6) can in principle be transformed into a linear program and then solved by conventional linear programming solvers. However, such solvers are not tailored for the matrix involved in the equality constraints that is large-scale and completely dense. For the same reason, methods that involves the inversion of such kind of matrices are not proper choices. In fact, this kind of problem is often solved by regularization, that is

$$\min \|u\|_{TV} + \frac{\lambda}{2}\|Au - b\|_2^2. \tag{7}$$

We solve it inside the space $\{u : S_0 u = b_0\}$ but don't include $S_0 u = b_0$ in the penalty term in (7) because this condition effectively reduces the number of variables in u.

The unconstrained convex optimization problem (7) is easier to solve than (6). Because (7) allows the constraint (4) to be relaxed, it can be used when the measurement b is contaminated by encoding errors such as noise. However, when there are no encoding errors, one must assign a large value to heavily weigh the fidelity term in order for the equality constraint to be nearly satisfied. Indeed, one can easily show that the solution of (7) never exactly equals the solution of (6) except for trivial cases. In this paper we will address two iterative algorithms to find a solution of (6) by solving a small number of instances of the unconstrained problem (7). The first scheme is based on the Bregman iterative regularization, which was introduced in [19] for the purpose of image denoising. The second scheme is based on the continuation method. The two methods share a similar algorithmic structure and only differ in one line, even though they are developed from different motivations.

We want to point out that the mathematical model that has a form like (6) or (7) has been widely discussed in recent references for different problems. For example, in [20] Candés *et al.* point out the connection between the tomography reconstruction with limited data and the total variation minimization problem with the measurement as linear constraints. In the context of compressed sensing the following optimization problem is discussed:

$$\min \|u\|_1 \quad \text{s.t.} \quad Au = b \tag{8}$$

where A is a measurement matrix. Here the regularization term is the l_1 norm of the desired signal u instead of the total variation. Another example is the ROF model for deblurring image that considers the following objective function:

$$\min \|u\|_{TV} + \frac{\lambda}{2}\|Ku - b\|_2^2 \tag{9}$$

where K is the blurring operator. In both cases, several efficient algorithms have been developed, see, e.g., [21]–[24]. The Bregman iterative scheme has received considerable attention in these fields as well. For example, it was extended to wavelet-based denoising [25] and compressed sensing in MR imaging [26]. In [21], the Bregman iteration for l_1 minimization problem is discussed, while an analogy for the total variational norm is covered briefly. In [21] and [22] a modified Bregman iteration called linearized Bregman iteration is developed for l_1 minimization problem. In a recent work [27] it was pointed out that the Bregman iterative regularization coincides with the classical Uzawa method. The continuation method has been used in these fields, for example, in [23].

To solve the unconstrained problem (7), we use the forward-backward operating splitting method in this paper, which was first proposed by Lions and Mercier [28] and Passty [29] in 1979. Subsequently this scheme and its modifications have been extensively studied by various groups (see [30] for related references). In a recent paper [30], Combettes and Wajs gave an extensive generalization of the forward-backward operating splitting method and proved the convergence in a relatively weak restriction on the objective function. More recently a large number of methods substantially equivalent to the operator splitting method have been developed to solve problem (9) through different approaches such as soft thresholding or linearization. They include (but are not limited to) [31]–[35]. The splitting method has been used to solve (8) as well, see, e.g., [36]–[38].

In Section II-C, we review the operator splitting method and apply it to problem (7). We also discuss its connection with the iterative method for equally sloped tomography introduced in

[6]. In Section II-D, we introduce the Bregman iterative method. In Section II-E we present the continuation method.

C. Operator Splitting Method

The operator splitting method was developed to solve the optimization problem when the objective function is the sum of two convex functions. Consider two proper lower semi-continuous convex functionals $J(u)$ and $H(u)$ defined in an Euclid space Ω such that $H(u)$ is differentiable with a Lipschitz continuous gradient, solving the optimization problem $\min[J(u)+H(u)]$ is equivalent to find u such that $0 \in \partial J(u) + \partial H(u)$, where ∂J denotes the sub-derivative of J when J is not differentiable. For $\tau > 0$, if $I + \tau\partial J$ is invertible, then we have the following iterative fixed-point algorithm:

$$v^n = (I - \tau\partial H)u^n \tag{10}$$

$$u^{n+1} = \arg\min_u \tau J(u) + \frac{1}{2}\|u - v^n\|_2^2. \tag{11}$$

Step (10) is called the forward step and the step (11) is called the backward step. The algorithm converges if $I - \tau\partial H$ is non-expensive [30].

Equations (10) and (11) can be applied to the problem (7) by letting $J(u) = (1/\lambda)\|u\|_{TV}$ and $H(u) = (1/2)\|Au - b\|_2^2$. Now the forward step (10) becomes

$$v^n = u^n - \tau A^\top(Au^n - b). \tag{12}$$

When $J(u) = (1/\lambda)\|u\|_{TV}$, the backward step (11) coincides with a standard ROF denoising model [17]

$$u^{n+1} = \arg\min_u \frac{\tau}{\lambda}\|u\|_{TV} + \frac{1}{2}\|u - v^n\|_2^2. \tag{13}$$

Due to the popularity of the ROF model, a number of fast algorithms have been developed to solve (13), e.g., the graph cut based solver [39], [40]. In the following we will use:

$$u^{n+1} = \mathrm{ROF}_{\tau/\lambda}(v^n) \tag{14}$$

to denote the procedure of solving (13). Note that both (12) and (14) are automatically restricted in the space $\{u : S_0 u = 0\}$. Putting them together, we obtain the following algorithm 1 to solve (7). As described in Section II-A, the algorithm can be easily generalized by replacing the $J(u)$ with other regularization functional, and the ROF solver in (14) with the corresponding solver.

Algorithm 1 Operator Splitting method for solving the unconstrained problem (7)

Initialize: $u \in \{u : S_0 u = b_0\}$.

while "$\|Au^n - b\|$ not converge" **do**

$v \leftarrow u - \tau A^\top(Au - b)$

$u \leftarrow \mathrm{ROF}_{\tau/\lambda}(v)$

end while

The computational complexity of the algorithm is low because $\mathcal{F}$ and $\mathcal{F}^\top$ and the ROF solver can be implemented very efficiently [10], [39]. Projections S and S_0 are costless elementary operators.

In practice, however, there are other physical constraints on u such as the non-negativity of the signal. This kind of physical constraints can be implemented in our algorithm by setting the negative part of u to zero in each iteration, which is equivalent to adding an extra penalty term on the negative part of u into $H(u)$. We will return to this in Section III.

Remark 1: In [6], an iterative algorithm is presented for image reconstruction through equally-sloped tomography, which is very similar to 1. After re-organization, the algorithm in [6] can be stated as follows:

Algorithm 2 Algorithm in [6] after organization, using our notations

Initialize: $u \in \{u : S_0 u = 0\}$. $A = S\mathcal{F}(I - S_0)$.

while "$\|Au - b\|$ not converge" **do**

$v \leftarrow u - (I - S_0)\mathcal{F}^{-1}(Au - b)$

$u \leftarrow \mathrm{ROF}_{1/\lambda}(v)$

end while

Compared to algorithm 1, algorithm 3 sets $\tau = 1$ and uses $\mathcal{F}^{-1}$ instead of $\mathcal{F}^\top$. This can be understood that algorithm 3 tries to converge the same minimum by using a different descent strategy. However, as we discussed in Section II-A, the computational cost of $\mathcal{F}^{-1}$ is almost 20 times higher than that of $\mathcal{F}^\top$. Our experimental results have shown that this difference makes algorithm 1 significantly faster than algorithm 3.

D. Bregman Iterative Regularization

The Bregman iteration was introduced in the context of image denoising by Osher *et al.* [19] and has recently been extended to other applications. Instead of minimizing $J(u) + H(u)$ where $J(u)$ is a regularization term and $H(u)$ is a fidelity term, the Bregman iterative method considers a series of minimization problems

$$u^{k+1} = \arg\min_u J(u) - J(u^k) - \langle \partial J(u^k), u - u^k\rangle + H(u) \tag{15}$$

starting with $u^0 = \partial J(u^0) = 0$, where $D(u, v) := J(u) - J(v) - \langle \partial J(v), u - v\rangle$ is called the Bregman distance [41]. In [19], it is proved that if $J(u)$ is convex and $H(u)$ is convex and differentiable, then the sequence $\{u^k\}$ given by iteration (15) monotonically decreases to the minimum of $H(u)$. Specifically, if $H(u) = \|Au - b\|_2^2$ and $\{u : Au = b\}$ is not empty, then $\{u^k\}$ converges to $\bar{u} \in \{u : Au = b\}$. Moreover, $\bar{u}$ solves the constrained problem

$$\min_u J(u) \quad \text{s.t.} \quad Au = b \tag{16}$$

where A is a linear operator and in our case $A = S\mathcal{F}(I - S_0)$. In other words, the iteration (15) tries to solve a constrained

optimization problem by solving a sequence of unconstrained problems.

Step (15) itself appears complicated, but if $H(u) = (\lambda/2)\|Au-b\|_2^2$, (15) is equivalent to the following iterative procedure [19] after simple algebraic manipulation:

$$u^k = \arg\min_u J(u) + \frac{\lambda}{2}\|Au - b^k\|_2^2 \tag{17}$$

$$b^{k+1} = b^k + b - Au^k \tag{18}$$

with initial setting $b^0 = b$. This procedure has an intriguing interpretation at first glance: in step (18) the residual $b - Au^{k+1}$ is "added back" to b^k, while b^k is used as the new "data" in the fidelity term in (17). Intuitively, this can be understood as we want to keep extracting "good" information from the residual in each iteration by adding the residual back to the data term. Numerical results show that this mechanism works very well. On the other hand, one can see from (17) that in each iteration, the unconstrained optimization keeps the same form as the original one, which means we can still use algorithm 1 to solve (17) in each step. This leads to algorithm 3.

Algorithm 3 Using Bregman iterative regularization to solve the constrained problem (6)

Initialize: $u \in \{u : S_0 u = 0\}$. Denote $A = S\mathcal{F}(I - S_0)$.

while "$\|Au - b\|$ not small enough (or other stop criteria)" **do**

  Start from $\tilde{b} = b$

  while "$\|Au - \tilde{b}\|$ not converge" **do**

    $v \leftarrow u - \tau A^\top(Au - \tilde{b})$

    $u \leftarrow \mathrm{ROF}_{\tau/\lambda}(v)$

  end while

  $\tilde{b} \leftarrow \tilde{b} + b - Au$

end while

Remark 2: In recent work [27], it was realized that the Bregman iterative regularization coincides with the classical Uzawa method, which basically is a gradient ascent method that solves the duality of the primal constrained optimization problem. An introduction of this method can be found in a standard optimization textbook, for example [42]. Let us consider the following constrained problem

$$\min_u \tilde{J}(u) \quad \text{s.t.} \quad Au = b. \tag{19}$$

The duality of the problem is $\max_v L(v)$ where

$$L(v) := \min_u \tilde{J}(u) + \langle v, Au - b\rangle. \tag{20}$$

Therefore, a natural gradient ascent for v on $L(v)$ leads to the following algorithm:

$$\begin{cases} u^k = \arg\min_u \tilde{J}(u) + \langle v^k, Au - b\rangle \\ v^{k+1} = v^n + \tau\partial L(v^k) = v^n + \tau(Au^k - b). \end{cases} \tag{21}$$

By setting $\tau = 1$ and $\tilde{J}(u) = J(u) + (1/2)\|Au\|_2^2$, the iteration (21) is essentially equivalent to (17). The difference between $J(u)$ and $\tilde{J}(u)$ is not important because the solution of (6) satisfies $Au = b$, and the extra term $(1/2)\|Au\|_2^2$ is a constant.

E. Continuation Method

This method is canonical in the context of equality constrained optimization, which was first proposed by Courant in 1943. It can be found in a standard textbook such as [43], in which it is called the quadratic penalty method. The main idea of this method is to solve the constrained problem (6) by a sequence of unconstrained problem (7), while gradually increasing the compromise parameter λ in (7). There is a theoretical result stating that when $\lambda \to \infty$, the solution of (7) converges to the solution of (6). In practice, directly choosing a very large λ in (7) will make the problem difficult to solve. Indeed, in this case, the fidelity term $H(u)$ will converge too fast and there is no room for $J(u)$ to be minimized. Instead, we first start from a smaller λ and solve (6). After it converges, we increase λ and use the current u as the new initial guess. This leads to the following algorithm 4.

Algorithm 4 Using continuation method to solve the constrained problem (6)

Initialize: $u \in \{u : S_0 u = 0\}$. Denote $A = S\mathcal{F}(I - S_0)$.

while "$\|Au - b\|$ not small enough (or other stop criteria)" **do**

  while "$\|Au - b\|$ not converge" **do**

    $v \leftarrow u - \tau A^\top(Au - b)$

    $u \leftarrow \mathrm{ROF}_{\tau/\lambda}(v)$

  end while

  $\lambda \leftarrow \lambda + \Delta\lambda$

end while

One can easily see that algorithms 3 and 4 share a very similar structure.

III. Implementation

Algorithm 3 can be easily implemented due to the concise structure. However, we need to address some details of the implementation. There are two major considerations. First, we want to have a good performance and fast convergence. Second, we want to minimize the number of parameters that we need to tune up in practice.

A. Precondition

As a well known fact, the efficiency of a gradient descent method for quadratic function depends heavily on the condition number of the matrix involved in the function, which, in our case, is $A = S\mathcal{F}(I - S_0)$. Although the condition number of this matrix is not easy to estimate, we can intuitively see that it is related to the condition number of $\mathcal{F}$. Unlike the standard Cartesian Fourier transform, the condition number of $\mathcal{F}$ is not equal to 1. As described in [10], the condition number of $\mathcal{F}$ is much greater than 1 because the pseudo-polar grid points have different intensity and weights in the frequency domain. To fix this problem, we use a preconditioner M, which is chosen such

that the condition number of $A^\top MA$ is much smaller than $A^\top A$ or at least the eigenvalues of $A^\top MA$ are well-clustered. Therefore, instead of considering $H(u) = \|Au - b\|_2^2$, we consider $H(u) = \|Au - b\|_M^2 = (Au - b)^\top M(Au - b)$ in our algorithm. Here, we use the diagonal preconditioner M established by the principal of density compensation, where each element of M is defined by the area of the sample square of the corresponding pseudo-polar grid in the frequency domain. This preconditioner has been used in [10] when calculating the inverse of $\mathcal{F}$ through the preconditioned conjugate gradient method. Since $A = S\mathcal{F}(I - S_0)$ and $S^\top MS = MS$ when M is diagonal, the corresponding line in algorithm 3 becomes

$$v^n = u^n - \tau A^\top M(Au - b) \tag{22}$$

which can be implemented efficiently.

B. Step Size

To make sure that the operator splitting iterative algorithm (10) and (11) converges, the step size τ in (10) should be chosen such that $I - \tau\partial H$ is contractive [30]. In our case where $H(u) = (Au - b)^\top M(Au - b)$, this means that

$$\left\|\left(u_1 - \tau A^\top M(Au_1 - b)\right) - \left(u_2 - \tau A^\top M(Au_2 - b)\right)\right\| < \|u_1 - u_2\| \tag{23}$$

which leads to the following universal condition on τ

$$0 < \tau < \frac{2}{\lambda_{\max}(A^\top MA)} \tag{24}$$

However, this is just a sufficient condition for fixed τ. In practice, to accelerate the convergence of $H(u)$, we may choose different τ in each step such that $H(u)$ is decreased fastest. Indeed, we can use a standard line search scheme to select the optimized τ. Since the direction of each step is given explicitly and H is a quadratic function, the optimal τ has a closed form that can be calculated precisely as follows:

$$\begin{aligned}\tau_u &:= \arg\min_\tau H\left(u - \tau A^\top M(Au - b)\right) \\ &= \frac{\left\|A^\top M(Au - b)\right\|_2^2}{\left\|AA^\top M(Au - b)\right\|_M^2}.\end{aligned} \tag{25}$$

Numerical results have shown that this choice of τ in each iteration gives very good convergence rate.

C. Parameter λ

For the Bregman iterative method, parameter λ in the ROF solver is not a crucial factor because after the Bregman iteration the solution converges to the constrained problem (6), in theory the choice of λ should not make difference. In practice we suggest a small initial λ. Numerical results also indicate that it is not a sensitive parameter. For the continuation method, a small initial λ should be chosen to make the image regularized enough at the very beginning. In each outer iteration, λ is increased by $\Delta\lambda$. This increment is not a sensitive factor as shown from the numerical experiments.

D. Stop Criteria

In algorithms 3 and 4, there are two levels of iterations, each of which needs an appropriate stop criterion. For the inner loop, i.e., the forward-backward operator splitting iteration, the iteration can be terminated when the relative decrease of $H(u)$ is smaller than a certain threshold, or after a fixed number of iterations. For the outer loop, very few iterations are needed. Numerical experiments show that generally 2–3 iterations can give good performance, which is consistent with the observations in [19] and [37] where different algorithms with similar structure are studied. We can also set a threshold of the residual $H(u)$ to automatically terminate the iteration. As discussed in Sections II-D and Sections II-E, the purpose of the outer loop is to iteratively "squeeze" information from the measurements. Too many outer iterations will introduce high noise into the image, especially when the measurements contain significant noise. Since the details and artifacts are brought back to the image gradually, under certain environments we can also let users judge the quality of images after each outer iterative step and terminate the outer iteration at a proper time.

On the other hand, as we want the final image to be faithful to the measured data, i.e., (4) is strictly satisfied, we apply a post "legitimation" procedure by correcting the measured Fourier coefficients of the image in frequency domain. Since the image has converged to a less noisy state during the previous steps, this final step will not bring back a lot of noise (although the image may be degraded if the data itself is noisy).

E. Overall Algorithm

Combining all things together, we can obtain algorithm 5 in which we insert physical positivity constraints on u and improve the performance as discussed in Section II-C. We also want to point out that this algorithm can be easily extended by replacing the ROF solver with other schemes that can regularize images in a certain manner, or by adding other physical constraints if we have the prior knowledge.

Algorithm 5 Final iterative algorithm for solving the constrained problem (6)

Initialize: $u \in \{u : S_0 u = 0\}$. Denote $A = S\mathcal{F}(I - S_0)$.

while "$\|Au - b\|$ not small enough (or other stop criteria)" **do**

  Start from $\tilde{b} = b$

  while "$\|Au - \tilde{b}\|$ not converge" **do**

    $\tau \leftarrow \|A^\top M(Au - b)\|_2^2 / \|AA^\top M(Au - b)\|_M^2$

    $v \leftarrow u - \tau A^\top M(Au - b)$

    $u \leftarrow \mathrm{ROF}_{\tau/\lambda}(v)$

    $u \leftarrow u_+$

  end while

  $\tilde{b} \leftarrow \tilde{b} + b - Au$ **or** $\lambda \leftarrow \lambda + \Delta\lambda$

end while

Remark 3: We now discuss the computational complexity of algorithm 5. In algorithm 5, there are three operators with the highest computational cost: the pseudo-polar Fourier transform $\mathcal{F}$, its adjoint operator $\mathcal{F}^\top$, and the ROF solver. In [10], the

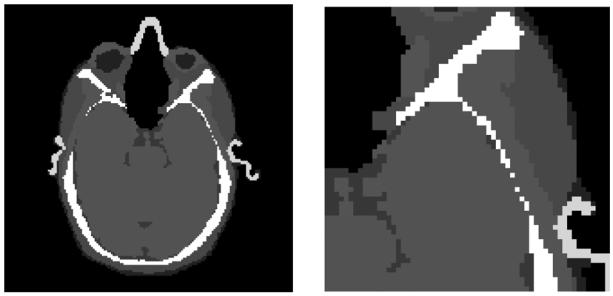

Fig. 2. (a) Slice 82 of the Zubal head phantom with assigned linear attenuation coefficients. (b) Zoomed-in view of the phantom showing fine features.

computational complexity as $\mathcal{F}$ and $\mathcal{F}^\top$ has been proven to be $O(n^2 \log n)$, i.e., in the same order of the standard 2-D FFT. In [23], [39] an efficient ROF solver has been proposed with computational complexity $O(n^2 \log n)$ as well. On the other hand, in each iteration only two times $\mathcal{F}$ and one time $\mathcal{F}^\top$ are virtually needed if we take advantage of the repetitive operator sequences in the algorithm. Therefore, the whole algorithm can be implemented very efficiently.

If we compare this algorithm with the algorithm in [6], since we avoid the inverse pseudo-polar Fourier Transform $\mathcal{F}^{-1}$ in our algorithm which has a much higher computational complexity, the computational time in each iteration is largely reduced. Moreover, due to the more efficient convergence strategy, the total number of iterations is reduced as well. These improvements are numerically demonstrated in Section IV.

IV. Numerical Experiments

There are two factors that influence the quality of the reconstructed image and the radiation dose: the number of projections and the fluence of the illumination particles. The former determines how many measurements, i.e., linear constraints on the image, and the latter determines the magnitude of noise in the measurements. In the following we compare our algorithms with the conventional FBP approach as a function of projections and fluence. We show that our algorithms perform far better than FBP even using fewer projections and less fluence. In another word, our method can lead to great dose reduction without reducing the quality of the reconstructed images.

To quantify the quality of image reconstruction of our algorithms for complex objects, we present numerical simulations on slice 82 of the Zubal anthropomorphic head phantom [44], shown in Fig. 2(a). The values that were assigned to the organs represent x-ray attenuation coefficients corresponding to a TASMIP x-ray spectra calculated for 120 kvp and 2 mm resulting in a mean flux weighted energy of 56.4 kev. Fig. 2(b) shows a zoom-in view the phantom indicating the fine features for a comparison purpose. In the numerical simulations we calculated 360, 90, 60, 45 projections, respectively, and added Poisson noise to the projections with a fluence of 7.0×10^5 m^{-2}. The reconstructed images by FBP, the EST iterative method given in [6] (i.e., EST iterative), the EST Bregman iterative method (i.e., EST Bregman) and the EST continuation method (i.e., EST continuation) are shown in Fig. 4. The arrows indicate the fine features that disappear in Fig. 3(i) and (m), but clearly

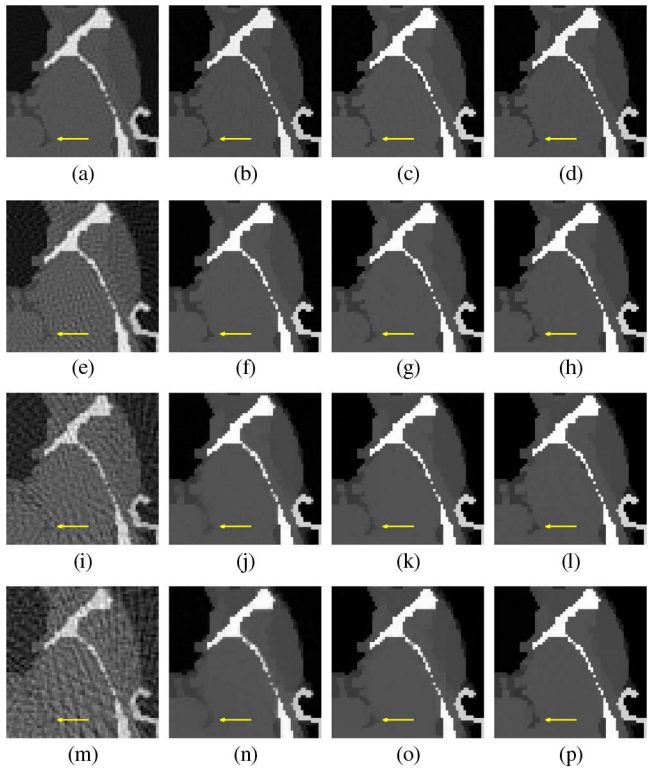

Fig. 3. Image reconstructions with a fluence of 7.0×10^5. First column (a), (e), (i), (m): FBP reconstructions from 360, 90, 60, and 45 projections, respectively. Second column (b), (f), (j), (n): EST iterative reconstructions from 360, 90, 60, and 45 projections, respectively. Third column (c), (g), (k), (o): EST continuation reconstructions from 360, 90, 60 and 45 projections, respectively. Last column (d), (h), (l), (p): EST Bregman reconstructions from 360, 90, 60, and 45 projections, respectively.

visible in the EST reconstructions from the same number of projections [Fig. 3(j), (k), (l), (n), (o) and (p)].

To quantify the reconstructions, we utilize the Fourier Ring Correlation (FRC) to measure the correlation of the reconstructed images to the original phantom as a function of spatial frequency [8]. The FRC across "rings" in Fourier domain is defined as

$$\mathrm{FRC}_{\mathrm{img1},\mathrm{img2}}(k,\Delta k) := \left.\frac{\left|\sum_\kappa F_{\mathrm{img1}}(\kappa) F^*_{\mathrm{img2}}(\kappa)\right|}{\sqrt{\sum_\kappa |F_{\mathrm{img1}}(\kappa)|^2 \sum_\kappa |F_{\mathrm{img2}}(\kappa)|^2}}\right|_{|\kappa|\in(k,k+\Delta k)} \tag{26}$$

where k is the radial parameter in Fourier domain, Δk the frequency interval size of the rings, and the subscripts refer to the reconstructed image and the original phantom, respectively. A FRC value of 1 represents 100% correlation while a value of 0 represents 0% correlation; the spatial frequency defined by the 0.5 value of the FRC curve, representing 50% correlation between reconstructed image and the original phantom, is commonly taken as a numerical value of the resolution. Fig. 4(a)–(d) show the FRC values of the FBP, EST iterative, EST continuation and EST Bregman reconstructions from 360, 90, 60, and 45 projections, respectively.

According to Figs. 3 and 4, the quality of reconstructed images with the EST methods is significantly better than FBP.

TABLE I
COMPUTATION TIME COMPARISON WITH A FLUENCE OF 7.0×10^5 m^{-2}

Computation time in seconds with a 2.40GHz Core 2 Duo CPU and a MATLAB environment				
	360 projections	90 projections	60 projections	45 projections
FBP method	5.27	1.46	0.95	0.77
EST iterative method in [6]	80.06	176.78	214.03	283.14
EST Continuation method	45.10	80.06	92.68	126.15
EST Bregman method	39.54	50.58	77.67	95.86
Total invoking times of the PPFFT / the adjoint PPFFT / the inverse PPFFT				
	360 projections	90 projections	60 projections	45 projections
EST iterative method in [6]	20/0/20	44/0/44	64/0/64	83/0/83
EST Continuation method	42/21/0	100/50/0	116/58/0	138/69/0
EST Bregman method	36/18/0	46/23/0	80/40/0	102/51/0

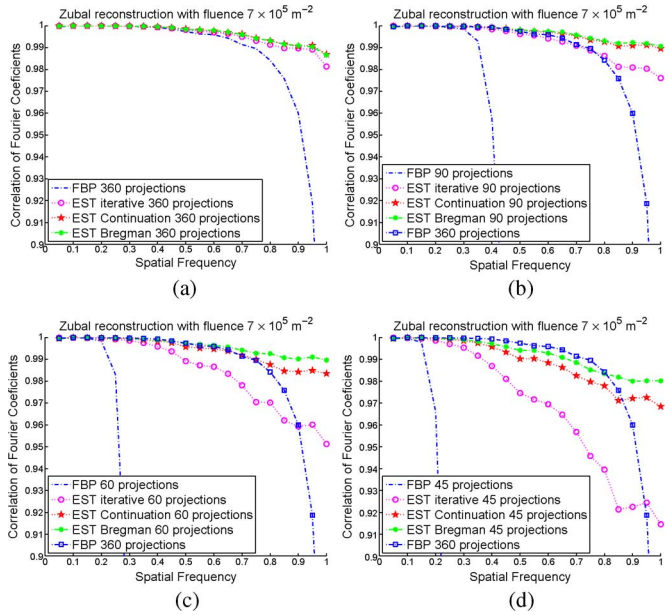

Fig. 4. Quantitative FRC comparisons of the reconstructions (Fig. 3) by the four method from (a) 360 projections, (b) 90 projections, (c) 60 projections, and (d) 45 projections, respectively.

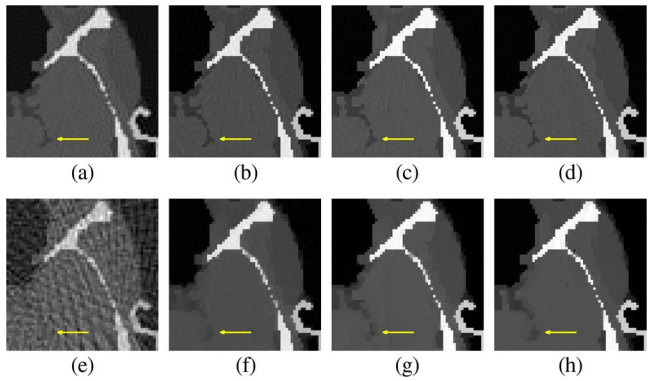

Fig. 5. Image reconstructions with a fluence of 3.5×10^5. (a), (e) FBP reconstructions from 360 and 45 projections. (b), (f) EST iterative reconstructions from 360 and 45 projections. (c), (g) EST continuation reconstructions from 360 and 45 projections. (d), (h) EST Bregman reconstructions from 360 and 45 projections.

As Fig. 4 shows, with the same number of projections, the EST methods outperform FBP in all spatial frequencies, indicating higher resolution and correlation for the EST reconstructions. The differences between the three EST methods are relatively small when the number of projections is large, but becomes large when the number of projections is reduced. Furthermore, when there is a limited number of projections, the EST Bregman reconstruction shows more fine features that the EST iterative reconstruction, as shown in Fig. 3(n), (o), and (p). The improvement is mainly due to the outer iterative loop in the EST Bregman and continuation algorithms, which can obtain fine features from noisy data more efficiently. As importantly, by replacing $\mathcal{F}^{-1}$ with $\mathcal{F}^{\top}$, the computational time in each iteration is reduced by approximately 70% in average, and the total number of iterations is reduced by approximately 40% in average due to the more efficient convergence strategy. Therefore, even with the extra outer iterative loop in the new algorithms, the overall computation time is significantly reduced, shown in Table I. Although the new algorithms still require more computation power than FBP, they can in principle be implemented in clinical CT scanners by parallel computing and fast FFT based processors such as graphical processing units (GPUs) [45].

According to Figs. 3(a) and (p) and 4(d), the EST Bregman reconstruction from 45 projections is as good as the FBP reconstruction from 360 projections. We also performed dose reduction numerical experiments by reducing the fluence. Fig. 5 shows the FBP, EST iterative, EST continuation and EST Bregman reconstructions from 360 and 45 projections with a fluence of 3.5×10^5, respectively. The EST Bregman reconstruction from 45 projections [Fig. 3(h)] is still comparable to the FBP reconstruction from 360 projections [Fig. 3(a)]. The significant dose reduction of the EST method is mainly due to the fact that it doesn't interpolate the missing projections from the measurements, but directly searches for the "best" image from the acquired measurements by using advanced iterative algorithms. Although there exist other iterative algorithm for tomographic reconstruction such as ART, SART and SIRT, our previous quantitative comparisons have shown that the EST iterative method is far superior [5], [6]. Therefore, in this paper, we mainly focus on the quantitative comparisons between the EST iterative method with the new algorithms.

V. CONCLUSION

We show that the EST reconstruction can be represented as a constrained problem (6), and develop an iterative approach to find the solution by solving a sequence of unconstrained

problems (7). We establish the operator splitting method to efficiently and accurately solve (7). Based on these mathematical developments, we propose two new iterative algorithms for image reconstruction through EST, which are called the EST Bregman and the EST continuation algorithms. Compared to the traditional FBP, ART, and SART, the new image reconstruction algorithms avoid any direct interpolations and search for the most regularized image that is consistent with the experimental measurements and the physical constraints. Compared to the EST iterative algorithm reported in [6], the EST Bregman and the EST continuation algorithms not only improve the image quality, but also significantly reduce the computational time. Our numerical experiment results suggest that EST coupled with the novel iterative algorithm significantly reduce the required radiation dose for achieving a desired resolution. We expect the new algorithms can be broadly applied to X-ray tomography, electron microscopy, coherent diffraction microscopy and other tomographic fields.

REFERENCES

[1] J. Miao, F. Förster, and O. Levi, "Equally sloped tomography with oversampling reconstruction," *Phys. Rev. B*, vol. 72, no. 5, p. 52103, 2005.

[2] J. Miao, C. Chen, C. Song, Y. Nishino, Y. Kohmura, T. Ishikawa, D. Ramunno-Johnson, T. Lee, and S. Risbud, "Three-dimensional GaN-Ga2O3 core shell structure revealed by x-ray diffraction microscopy," *Phys. Rev. Lett.*, vol. 97, no. 21, p. 215503, 2006.

[3] J. Miao, T. Ishikawa, Q. Shen, and T. Earnest, "Extending X-ray crystallography to allow the imaging of noncrystalline materials, cells, and single protein complexes," *Annu. Rev. Phys. Chem.*, vol. 59, p. 387, 2008.

[4] C. Chen, J. Miao, and T. Lee, "Tomographic image alignment in three-dimensional coherent diffraction microscopy," *Phys. Rev. B*, vol. 79, p. 052102, 2009.

[5] E. Lee, B. Fahimian, C. Iancu, C. Suloway, G. Murphy, E. Wright, D. Castaño-Díez, G. Jensen, and J. Miao, "Radiation dose reduction and image enhancement in biological imaging through equally-sloped tomography," *J. Struct. Biol.*, vol. 164, no. 2, pp. 221–227, 2008.

[6] B. Fahimian, A. Chatziioannou, Y. Mao, and J. Miao, Equally-Sloped Tomography and Its Applications to Radiation Dose Reduction in Transmission CT.

[7] A. Kak and M. Slaney, *Principles of Computerized Tomographic Imaging*. New York: IEEE, 1988, I. E. in Medicine, and B. Society.

[8] J. Frank, *Electron Tomography: Methods for Three-Dimensional Visualization of Structures in the Cell*. New York: Springer, 2006.

[9] F. Natterer, *The Mathematics of Computerized Tomography*. Philadelphia, PA: SIAM, 2001.

[10] A. Averbuch, R. Coifman, D. Donoho, M. Israeli, and Y. Shkolnisky, "A framework for discrete integral transformations I—The pseudopolar fourier transform," *SIAM J. Sci. Comput.*, vol. 30, pp. 785–803, 2008.

[11] A. Averbuch, R. Coifman, D. Donoho, M. Elad, and M. Israeli, "Fast and accurate polar Fourier transform," *Appl. Comput. Harmon. Anal.*, vol. 21, no. 2, pp. 145–167, 2006.

[12] J. Miao, D. Sayre, and H. Chapman, "Phase retrieval from the magnitude of the Fourier transforms of nonperiodic objects," *J. Opt. Soc. Amer. A*, vol. 15, no. 6, pp. 1662–1669, 1998.

[13] J. Miao, P. Charalambous, J. Kirz, and D. Sayre, "Extending the methodology of X-ray crystallography to allow imaging of micrometre-sized non-crystalline specimens," *Nature*, vol. 400, no. 6742, pp. 342–344, 1999.

[14] D. Sayre, "Some implications of a theorem due to Shannon," *Acta Cryst.*, vol. 5, no. 6, p. 843, 1952.

[15] R. Mersereau and A. Oppenheim, "Digital reconstruction of multidimensional signals from their projections," *Proc. IEEE*, vol. 62, no. 10, pp. 1319–1338, Oct. 1974.

[16] A. Averbuch, R. Coifman, D. Donoho, M. Israeli, Y. Shkolnisky, and I. Sedelnikov, "A framework for discrete integral transformations II—The 2D discrete Radon transform," *SIAM J. Sci. Comput.*, vol. 30, no. 2, pp. 785–803, 2008.

[17] L. Rudin, S. Osher, and E. Fatemi, "Nonlinear total variation based noise removal algorithms," *Phys. D*, vol. 60, no. 1–4, pp. 259–268, 1992.

[18] A. Buades, B. Coll, and J. Morel, "A review of image denoising algorithms, with a new one," *Multiscale Model. Simul.*, vol. 4, no. 2, p. 490, 2005.

[19] S. Osher, M. Burger, D. Goldfarb, J. Xu, and W. Yin, "An iterative regularization method for total variation based image restoration," *Multiscale Model. Simul.*, vol. 4, no. 2, pp. 460–489, 2005.

[20] E. Candes, J. Romberg, and T. Tao, "Robust uncertainty principles: Exact signal reconstruction from highly incomplete frequency information," *IEEE Trans. Inf. Theory*, vol. 52, no. 2, pp. 489–509, 2006.

[21] W. Yin, S. Osher, D. Goldfarb, and J. Darbon, "Bregman iterative algorithms for l_1-minimization with applications to compressed sensing," *SIAM J. Imag. Sci.*, vol. 1, no. 1, pp. 143–168, 2008.

[22] S. Osher, Y. Mao, B. Dong, and W. Yin, "Fast linearized bregman iteration for compressive sensing and sparse denoising," *Commun. Math. Sci.*, 2009.

[23] Y. Wang, J. Yang, W. Yin, and Y. Zhang, "A new alternating minimization algorithm for total variation image reconstruction," *SIAM J. Imag. Sci.*, vol. 1, pp. 248–272, 2008.

[24] L. He, A. Marquina, and S. Osher, "Blind deconvolution using TV regularization and Bregman iteration," *Int. J. Imag. Syst. Technol.*, vol. 15, no. 1, p. 74, 2005.

[25] J. Xu and S. Osher, "Iterative regularization and nonlinear inverse scale space applied to wavelet-based denoising," *IEEE Trans. Image Process.*, vol. 16, no. 2, p. 534, Feb. 2007.

[26] L. He, T.-C. Chang, and S. Osher, "MR image reconstruction from sparse radial samples by using iterative refinement procedures," in *Proc. 13th Annu. Meet. ISMRM*, 2006, p. 696.

[27] J. Cai, E. Candes, and Z. Shen, A Singular Value Thresholding Algorithm for Matrix Completion Oct. 2008 [Online]. Available: http://arxiv.org/pdf/0810.3286 [Online]. Available: http://arxiv.org/abs/0810.3286

[28] P. Lions and B. Mercier, "Splitting algorithms for the sum of two nonlinear operators," *SIAM J. Numer. Anal.*, vol. 16, p. 964, 1979.

[29] G. Passty, "Ergodic convergence to a zero of the sum of monotone operators in Hilbert space," *J. Math. Anal. Appl.*, vol. 72, no. 2, pp. 383–390, 1979.

[30] P. Combettes and V. Wajs, "Signal recovery by proximal forward-backward splitting," *Multiscale Model. Simul.*, vol. 4, no. 4, p. 1168, 2006.

[31] M. Figueiredo and R. Nowak, "Wavelet-based adaptive image deconvolution," presented at the IEEE Int. Conf. Acoustics, Speech, and Signal Processing, 2002.

[32] A. Chambolle, R. DeVore, N. Lee, and B. Lucier, "Nonlinear wavelet image processing: Variational problems, compression, and noise removal through wavelet shrinkage," *IEEE Trans. Image Process.*, vol. 7, no. 3, p. 319, Mar. 1998.

[33] I. Daubechies, M. Defrise, and C. De Mol, "An iterative thresholding algorithm for linear inverse problems with a sparsity constraint," *Commun. Pure Appl. Math.*, vol. 57, no. 11, pp. 1413–1457, 2004.

[34] M. Elad, B. Matalon, and M. Zibulevsky, "Coordinate and subspace optimization methods for linear least squares with non-quadratic regularization," *Appl. Comput. Harmon. Anal.*, vol. 23, no. 3, pp. 346–367, 2007.

[35] E. Hale, W. Yin, and Y. Zhang, "Fixed-point continuation for ℓ_1-minimization: Methodology and convergence," *SIAM J. Optim.*, vol. 19, p. 1107, 2008.

[36] Y. Wang, W. Yin, and Y. Zhang, Experimental Report of Fixed Point-Continuation for TotalVariation Minimization.

[37] X. Zhang, M. Burger, X. Bresson, and S. Osher, Bregmanized Nonlocal Regularization for Deconvolution and Sparse Reconstruction [Online]. Available: ftp://ftp.math.ucla.edu/pub/camreport/cam09-03.pdf

[38] J. Darbon and S. Osher, Fast Discrete Optimizations for Sparse Approximations and Deconvolutions preprint, 2007.

[39] D. Goldfarb and W. Yin, Parametric Maximum Flow Algorithms for Fast Total Variation Minimization [Online]. Available: http://www.caam.rice.edu/wy1/paperfiles/

[40] J. Darbon and M. Sigelle, "A fast and exact algorithm for total variation minimization," in *Proc. 2nd Iberian Conf. Pattern Recognition and Image Analysis*, 2005, vol. 3522, pp. 351–359, Springer.

[41] L. Bregman, "The relaxation method of finding the common point of convex sets and its application to the solution of problems in convex programming," *USSR Computational Mathematics and Mathematical Physics*, vol. 7, no. 3, pp. 200–217, 1967.

[42] I. Ekeland and R. Temam, *Convex Analysis and Variational Problems*. Philadelphia, PA: SIAM, 1999.
[43] J. Nocedal and S. Wright, *Numerical Optimization*. New York: Springer, 1999.
[44] I. Zubal, C. Harrell, E. Smith, Z. Rattner, G. Gindi, and P. Hoffer, "Computerized three-dimensional segmented human anatomy," *Med. Phys.*, vol. 21, p. 299, 1994.
[45] K. Moreland and E. Angel, "The FFT on a GPU," in *Proc. ACM SIGGRAPH/EUROGRAPHICS Conf. Graphics Hardware*, Switzerland, 2003, pp. 112–119, Eurographics Association Aire-la-Ville, Switzerland.

Yu Mao, photograph and biography not available at the time of publication.

Benjamin P. Fahimian, photograph and biography not available at the time of publication.

Stanley J. Osher received the B.S. degree in mathematics from Brooklyn College, Brooklyn, NY, in 1962, and the M.S. and Ph.D. degrees in mathematics from New York University in 1964 and 1966, respectively.

He has been with the University of California, Los Angeles, since 1977. He is currently a Professor in the Department of Mathematics and the Director of Special Projects at the Institute for Pure and Applied Mathematics. He is the founder and CEO of Level Set Systems, Inc., and has cofounded two other companies. He was an invited speaker at the 1994 International Congress of Mathematics and an ISI Original Highly Cited Researcher.

Dr. Osher received the 2002 Computational Mechanics Award from the Japan Society of Mechanical Engineers, the 2003 ICIAM Pioneer Prize, and the 2005 SIAM Kleinman Prize. He was elected to the National Academy of Sciences in 2005.

Jianwei Miao, photograph and biography not available at the time of publication.